

---

# DO DIFFERENT TRACKING TASKS REQUIRE DIFFERENT APPEARANCE MODELS?

---

<b>Zhongdao Wang</b> Tsinghua University wcd17@mails.tsinghua.edu.cn	<b>Hengshuang Zhao</b> University of Oxford hengshuang.zhao@eng.ox.ac.uk	<b>Ya-Li Li</b> Tsinghua University liyali13@tsinghua.edu.cn
<b>Shengjin Wang</b> <sup>*</sup> Tsinghua University wgsgj@tsinghua.edu.cn	<b>Philip H.S. Torr</b> University of Oxford philip.torr@eng.ox.ac.uk	<b>Luca Bertinetto</b> FiveAI luca.bertinetto@five.ai

## ABSTRACT

Tracking objects of interest in a video is one of the most popular and widely applicable problems in computer vision. However, with the years, a Cambrian explosion of use cases and benchmarks has fragmented the problem in a multitude of different experimental setups. As a consequence, the literature has fragmented too, and now the novel approaches proposed by the community are usually specialised to fit only one specific setup. To understand to what extent this specialisation is actually necessary, in this work we present **UniTrack**, a solution to address *five* different tasks within the same framework. UniTrack consists of a single and task-agnostic appearance model, which can be learned in a supervised or self-supervised fashion, and multiple “heads” to address individual tasks and that do not require training. We show how most tracking tasks can be solved within this framework, and that the *same* appearance model can be used to obtain performance that is competitive against specialised methods for all the five tasks considered. The framework also allows us to analyse appearance models obtained with the most recent self-supervised methods, thus significantly extending their evaluation and comparison to a larger variety of important problems. Code available at [this URL](#).

## 1 Introduction

Unlike popular image-based computer vision tasks such as classification and object detection, which are (for the most part) unambiguous and clearly defined, the problem of *object tracking* has been considered under different setups and scenarios, each motivating the design a separate set of benchmarks and methods. For instance, for the Single Object Tracking (SOT) and Video Object Segmentation (VOS) communities [32], [54], [82], *tracking* means estimating the location of an arbitrary user-annotated target object throughout a video, where the location of the object is represented by a bounding-box in SOT and by a pixel-wise mask in VOS. Instead, in multiple object tracking settings (MOT [47], MOTS [69] and PoseTrack [1]), tracking means connecting sets of (often given) detections across video frames to address the problem of identity association and form trajectories. Despite these tasks only differ in the number of objects per frame to consider and observation format (bounding boxes, keypoints or masks), the best practices developed by the methods tackling them vary significantly.

Though on the one hand the proliferation of setups, benchmarks and methods is surely positive in that it allows specific use cases to be thoroughly studied, we argue it makes increasingly harder to effectively study one of the fundamental problems that all these tasks have in common, *i.e.* *what constitutes a good representation to track objects throughout a video?* Successes in (self-supervised) pre-trained models for natural language processing [16], [67] and vision [9], [26] have suggested that a strong representation helps improve multiple down-stream tasks. Similarly, we speculate a good representation can probably benefit all tracking tasks, regardless of their setups. In order to validate our speculation, in this paper we present a framework that allows to adopt the same appearance model to address *five* different tracking tasks

---

<sup>\*</sup>Corresponding author

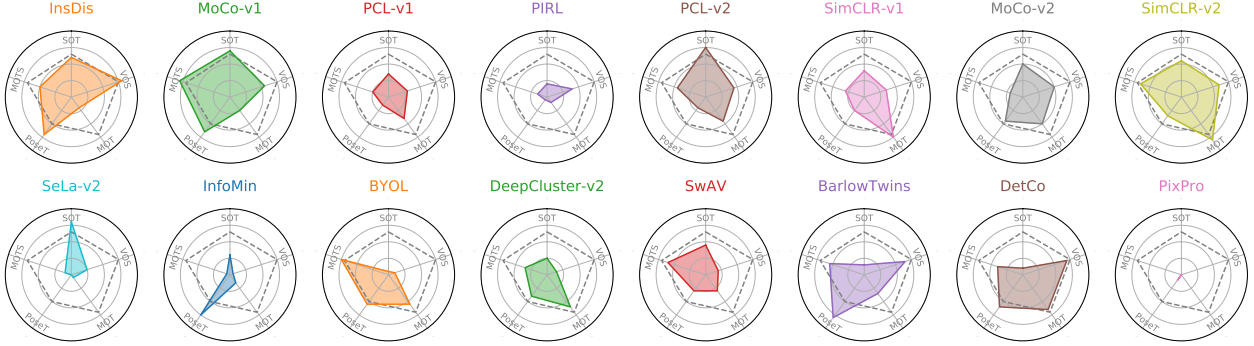


**Figure 1:** Radar charts of appearance model performance on five tracking tasks. We compute rankings in terms of AUC,  $\mathcal{J}$ -mean, IDF-1, 1DF-1 for SOT, VOS, MOT, PoseTracking, and MOTS, respectively. A higher rank (better performance) corresponds to a vertex nearer the outer circle. Larger areas of the pentagons mean better overall performance. Results of a vanilla ImageNet-supervised model are indicated with a gray dashed line. Notice how the best self-supervised models (e.g. InsDis [83], MoCo [26], SimCLR-v2 [10]) outperform ImageNet features on some tasks, but never on all of them.

(Figure 2). In our taxonomy (Figure 4), we consider existing tracking tasks as problems that have either *propagation* or *association* at their core. When the core problem is propagation (as in SOT and VOS), one has to localise a target object in the current frame given its location in the previous one. Instead, in association problems (MOT, MOTS, and PoseTrack), target states in both previous and current frames are given, and the goal is to determine the correspondence between the two sets of observations. We show how most tracking tasks currently considered by the literature can be simply expressed starting from the *primitive* of propagation or association. For propagation tasks, we employ existing box and mask propagation algorithms [5], [70], [73]. For association tasks, we propose a novel reconstruction-based metric that leverages fine-grained correspondence to measure similarities between observations.

In the proposed framework, each individual task is assigned to a dedicated “head” that allows to represent the object(s) in the appropriate format to compare against prior arts on the relevant benchmarks. Note that neither the components addressing the propagation and association primitives, nor the task-specific heads contain learnable parameters; only the base appearance model does. Importantly, we do not train appearance models on a single target task. Instead, we adopt task-agnostic supervised or self-supervised models popular in the community and that have already demonstrated their effectiveness across image-based tasks. This way, our work also serves the purpose of evaluating and comparing appearance models obtained from self-supervised learning approaches (see Figure 1) beyond the limited set of image-based problems typically seen in the literature.

To summarise, the contributions of our work are as follows:

- We propose UniTrack, a framework that supports five tracking tasks: SOT [82], VOS [54], MOT [47], MOTS [69], and PoseTrack [1]; and that can be easily extended to new ones.
- We show how UniTrack can leverage many existing general-purpose appearance models to achieve a performance that is competitive with the state-of-the-art on four out of the five tasks considered.
- We propose a novel reconstruction-based similarity metric for association that preserves fine-grained visual features and supports multiple observation formats (box, mask and pose).
- We perform an extensive evaluation of self-supervised models, significantly extending their empirical analysis to video-based tasks.

## 2 The UniTrack Framework

### 2.1 Overview

Inspecting existing tracking tasks and benchmarks, we noticed that their differences can be roughly categorised across four axes, illustrated in Figure 2 and detailed below.

1. Whether the requirement is to track a single object (SOT [32], [82], VOS [54]), or multiple objects (MOT [54], MOTS [69], PoseTrack [1]).
2. Whether the targets are specified by a user in the first frame only (SOT, VOS), or instead are given in every frame, e.g. by a pre-trained detector (MOT, MOTS, PoseTrack).

	Single object, user-specified	Multiple objects, detector-specified
Box	 Task: Single Object Tracking (SOT) Datasets: OTB-100, VOT-16/19 <i>Class-agnostic</i>	 Task: Multi-Object Tracking (MOT) Datasets: MOT challenge, KITTI <i>Class-specific</i>
Mask	 Task: Video Object Segmentation (VOS) Datasets: DAVIS-2016/2017 <i>Class-agnostic</i>	 Task: Multi-Object Tracking & Seg. (MOTS) Datasets: MOTS, KITTI-MOTS <i>Class-specific</i>
Pose	 Task: Pose Propagation Datasets: JHMDB <i>Class-specific</i>	 Task: Pose Tracking (PoseTrack) Datasets: PoseTrack-2017/2018 <i>Class-specific</i>

**Figure 2:** Existing tracking problems and their respective benchmarks differ from each other under several aspects: the assumption could be that there is a single or multiple objects to track; targets can be specified by the user in the first frame only, or assumed to be given at every frame (*e.g.* provided by a detector); the classes of the targets can be known (class-specific) or unknown (class-agnostic); the representation of the targets can be bounding boxes, pixel-wise masks, or pose annotations.

3. Whether the target objects are represented by bounding-boxes (SOT, MOT), pixel-wise masks (VOS, MOTS) or pose annotations (PoseTrack).
4. Whether the task is class-agnostic, *i.e.* the target objects can be of *any* class (SOT, VOS); or if instead they are from a predefined set of classes (MOT, MOTS, PoseTrack).

Typically, in single-target tasks the target is specified by the user in the first frame, and it can be of any class. Instead, for multi-target tasks detections are generally considered as given for every frame, and the main challenge is to solve identity association for the several objects. Moreover, in multi-target tasks the set of classes to address is generally known (*e.g.* pedestrians or cars).

Figure 3 depicts a schematic overview of the proposed UniTrack framework, which can be understood as conceptually divided in three “levels”. The first level is represented by the appearance model, responsible for extracting high-resolution feature maps from the input frame (Section 2.2). The second level consists of the two fundamental algorithmic building blocks addressing *propagation* (Section 2.3) and *association* (Section 2.4). Finally, the last level comprises multiple task-specific algorithms that make direct use of the primitives of the second level. In this work, we illustrate how UniTrack can be used to obtain competitive performance on all of the five tracking tasks of level 3 from Figure 3. Moreover, new tracking tasks can be easily integrated by using the framework and the primitives provided.

Importantly, note that the appearance model is the only component containing trainable parameters. The reason we opted for a shared and non task-specific representation is twofold. Firstly, the large amount of different setups motivated us to investigate whether having separately-trained models for each one is necessary. Since training on specific datasets can bias the representation towards a limited set of visual concepts (*e.g.* animals or vehicles) and limit its applicability to “open-world” settings, we wanted to understand how far can a shared representation go. Second, we wanted to provide the community with multiple baselines that can be used to better assess newly proposed contributions, and that can be immediately used on new datasets and tasks without the need of retraining.

## 2.2 Base appearance model

The base appearance model  $\phi$  takes as input a 2D image  $I$  and outputs a feature map  $X = \phi(I) \in \mathbb{R}^{H \times W \times C}$ . Since ideally an appearance model used for object propagation and association should be able to leverage fine-grained semantic correspondences between images, we choose a network with a small stride of  $r = 8$ , so that its output in feature space can have a relatively large resolution.

We refer to the vector (along the channel dimension) of a single point in the feature map as a point vector. We expect a point vector  $x_1^i \in \mathbb{R}^C$  from the feature map  $X_1$  to have a high similarity with its “true match” point vector  $\hat{x}_2^i$  in  $X_2$ ,

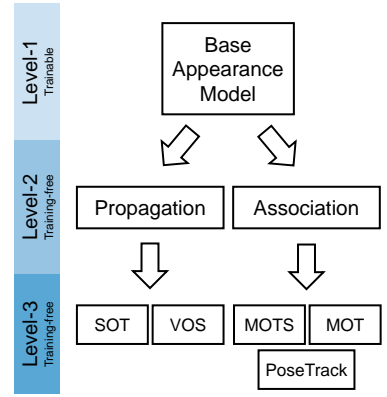


**Figure 3:** Overview of UniTrack. The framework can be divided in three levels. Level-1: a trainable base appearance model. Level-2: training-free algorithmic blocks. Level-3: training-free task-specific heads.

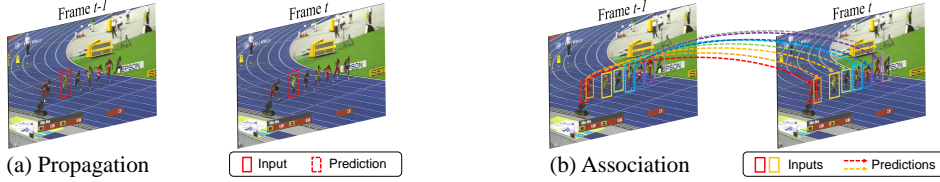


**Figure 4:** Propagation v.s. Association. In the *propagation* problem, the goal is to estimate the target state at the current frame given the observation in the previous one. This is typically addressed for one object at the time. In the *association* problem, observations in both previous and current frames are given, and the goal is to determine correspondences between the two sets.

while being far apart from all the “false match” point vectors  $x_2^j$  in  $X_2$ ; *i.e.* we expect  $s(x_1^i, x_2^i) > s(x_1^i, x_2^j), \forall j \neq i$ , where  $s(\cdot, \cdot)$  represents a similarity function.

In order to learn fine-grained correspondences, fully-supervised methods are only amenable for synthetic datasets (*e.g.* Flying Chairs for optical flow [17]). With real-world data, it is intractable to label pixel-level correspondences and train models in a fully-supervised fashion. To overcome this obstacle, in this paper we explore two possible solutions. The first is inspired by prior works that have pointed out how fine-grained correspondences emerge in middle-level features [44], [86]. Hence, a previously-trained model for classification or metric learning could serve us well as base appearance model. The second is inspired by recent progress in self-supervised learning approaches that specifically leverage pixel-wise pretext tasks [29], [70]. In this paper, we empirically explore which representations are best by measuring their performance on five different tracking problems.

### 2.3 Propagation

**Problem definition.** Figure 4a schematically illustrates the problem of *propagation*, which we use as a primitive to address SOT and VOS tasks. Considering the single-object case, given video frames  $\{I_t\}_{t=1}^T$  and an initial ground truth observation  $z_1$  as input, the goal is to predict object states  $\{\hat{z}_t\}_{t=2}^T$  for each time-step  $t$ . In this work we consider three formats to represent objects: bounding boxes, segmentation masks and pose skeletons.

**Mask propagation.** In order to propagate masks, we rely on the (attention-based) approach popularised by recent video self-supervised methods [29], [34], [39], [70]. Consider the feature maps of a pair of consecutive frames  $X_{t-1}$  and  $X_t$ , both in  $\mathbb{R}^{s \times C}$ , and the label mask  $z_{t-1} \in [0, 1]^s$  of the previous frame <sup>2</sup>, where  $s = H \times W$  indicates its spatial resolution. We compute the matrix of transitions  $K_{t-1}^t = [k_{i,j}]_{s \times s}$  as the affinity matrix between  $X_{t-1}$  and  $X_t$ . Each element  $k_{i,j}$  is defined as

$$k_{i,j} = \text{Softmax}(X_{t-1}, X_t^\top; \tau)_{ij} = \frac{\exp(\langle x_{t-1}^i, x_t^j \rangle / \tau)}{\sum_k^s \exp(\langle x_{t-1}^i, x_t^k \rangle / \tau)}, \quad (1)$$

where  $\langle \cdot, \cdot \rangle$  indicates inner product, and  $\tau$  is a temperature hyperparameter. As in [29], we only keep the top- $K$  values for each row and set other values to zero. Then, the mask for the current frame at time  $t$  is predicted by propagating the previous prediction:  $z_t = K_{t-1}^t z_{t-1}$ . Mask propagation proceeds in a recurrent fashion: the output mask of the current frame is used as input for the next one.

**Pose propagation.** In order to represent pose keypoints, we use the widely adopted Gaussian *belief maps* [78]. For a keypoint  $p$ , we obtain a belief map  $z^p \in [0, 1]^s$  by using a Gaussian with mean equal to the keypoint’s location and variance proportional to the subject’s body size. In order to propagate a pose, we can then individually propagate each belief map in the same manner as mask propagation, again as  $z_t^p = K_{t-1}^t z_{t-1}^p$ .

**Box propagation.** The position of an object can also be more simply expressed with a four-dimensional vector  $z = (u, v, w, h)$ , where  $(u, v)$  are the coordinates of the bounding-box center, and  $(w, h)$  are its width and height.

Despite one could reuse the strategy adopted above by simply converting the bounding-box to a pixel-wise mask, we observed that using this strategy leads to inaccurate predictions. Instead, we use the approach of SiamFC [5], which consists in performing cross-correlation (XCORR) between the target template  $z_{t-1}$  and the frame  $X_t$  to find the new location of the target at frame  $t$ . Cross-correlation is performed at different scales, so that the bounding-box representation can be resized accordingly. We also provide a Correlation Filter-based alternative (DCF) [65], [73], which also does not involve any training (see Appendix A.1).

<sup>2</sup>Note this corresponds to the ground-truth initialisation when  $t = 1$ , and to the latest prediction otherwise.

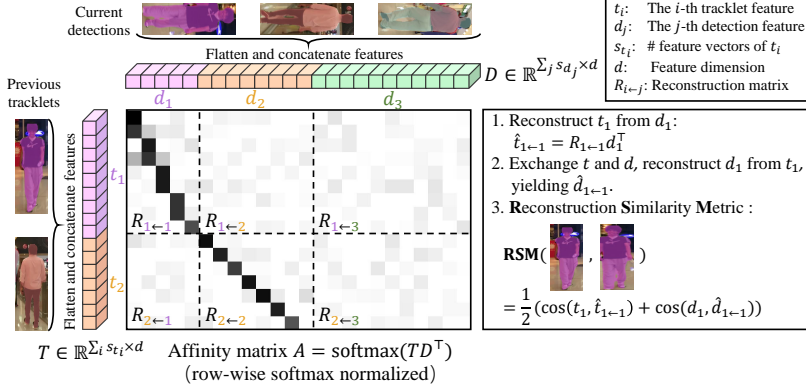


**Figure 5:** Illustration of the Reconstruction Similarity Metric. First, object-level features of existing tracklets and current detections are flattened and concatenated, respectively. Then an affinity matrix between the two feature sets is computed. For a pair of tracklet  $t_i$  and detection  $d_j$ , we “extract” the corresponding sub-matrix from the entire affinity matrix as linear weights and reconstruct  $t_i$  from  $d_j$  using these linear weights. The similarity between the original object-level feature and its reconstructed version is finally taken as the Reconstruction Similarity Metric. We want the metric to be symmetric, so we perform reconstruction both forward ( $t_i \leftarrow d_j$ ) and backward ( $t_i \rightarrow d_j$ ) and then compute average similarity.

## 2.4 Association

**Problem definition.** Figure 4b schematically illustrates the *association* problem, which we use to address the tasks of MOT, MOTS and PoseTrack. In this case, observations for object states  $\{\hat{\mathcal{Z}}_t\}_{t=1}^T$  are given for all the frames  $\{I_t\}_{t=1}^T$ , typically provided by a pre-trained detector. The goal here is to form trajectories by connecting observations across adjacent frames according to their identity.

**Association algorithm.** We adopt the association algorithm proposed in JDE [77] for MOT, MOTS and PoseTrack tasks, of which detailed description can be found in Appendix B. In summary, we compute an  $N \times M$  distance matrix between  $N$  already-existing tracklets and  $M$  “new” detections from the last processed frame. We then use the Hungarian algorithm [33] to determine pairs of matches between tracklets and detections with the distance matrix as input. To obtain the matrix of distances used by the algorithm, we compute the linear combination of two terms accounting for *motion* and *appearance* cues. For the former, we compute a matrix indicating how likely a detection corresponds to the object state predicted by a Kalman Filter [31].

For the latter, the appearance component is computed using visual features from observations across frames: a given frame is first processed by the base appearance model (Section 2.2) to obtain a frame-level feature map. Then, while object-level features corresponding to box and mask representations can be directly obtained by cropping frame-level feature maps, when an object is represented via a pose, it first needs to be converted to a mask (via a procedure described in Appendix B.2).

A key issue of this scenario is how to measure similarities between object-level features. We find existing methods limited. First, objects are often compared by computing the cosine similarity of average-pooled object-level feature maps [61], [103]. However, the operation of average inherently discards local information, which is important for fine-grained recognition. Approaches [20], [62] that instead to some extent do preserve fine-grained information, such as those computing the cosine similarity of (flattened) feature maps, do not support objects with differently-sized representation (situation that occurs for instance with pixel-level masks). To cope with the above limitations, we propose a reconstruction-based similarity metric that is able to deal with different observation formats, while still preserving fine-grained information.

**Reconstruction Similarity Metric (RSM).** Let  $\{t_i\}_{i=1}^N$  denote the object-level features of  $N$  existing tracklets,  $t_i \in \mathbb{R}^{s_{t_i} \times C}$  and  $s_{t_i}$  indicates the spatial size of the object, *i.e.* the area of the box or the mask representing it. Similarly,  $\{d_j\}_{j=1}^M$  denotes the object-level features of  $M$  new detections. With the goal of computing similarities to obtain an  $N \times M$  affinity matrix to feed to the Hungarian algorithm, we propose a novel reconstruction-based similarity metric (RSM) between pairs  $(i, j)$ , which is obtained as

$$\text{RSM}(i, j) = \frac{1}{2}(\cos(t_i, \hat{t}_{i-j}) + \cos(d_j, \hat{d}_{j-i})), \quad (2)$$

where  $\hat{t}_{i-j}$  represents  $t_i$  reconstructed from  $d_j$  and  $\hat{d}_{j-i}$  represents  $d_j$  reconstructed from  $t_i$ . In multi-object tracking scenarios, observations are often incomplete due to frequent occlusions. As such, directly comparing features between

incomplete and complete observations often fails because of misalignment between local features. Suppose  $d_j$  is a detection feature representing a half body of a person, while  $t_i$  a tracklet feature representing the holistic body of a person, if we directly compute similarity (*e.g.* using cosine metric), their similarity would probably be rather small. RSM addresses this issue by introducing the reconstruction step, which can be understood as an alignment procedure. After the reconstruction, the co-occurring part of point features are aligned, and accordingly the final similarity becomes more meaningful.

The reconstructed object-level feature map  $\hat{t}_{i \leftarrow j}$  is a simple linear transformation of  $d_j$ , *i.e.*  $\hat{t}_{i \leftarrow j} = R_{i \leftarrow j} d_j$ , where  $R_{i \leftarrow j} \in \mathbb{R}^{s_{t_i} \times s_{d_j}}$  is a transformation matrix obtained as follows. We first flatten and concatenate all object-level features belonging to a tracklet (*i.e.* the set of observations corresponding to an object) into a single feature matrix  $T \in \mathbb{R}^{(\sum_i s_{t_i}) \times C}$ . Similarly, we obtain all the object-level feature maps of a new set of detections  $D \in \mathbb{R}^{(\sum_j s_{d_j}) \times C}$ . Then, we compute the affinity matrix  $A = \text{Softmax}(TD^\top)$  and “extract” individual  $R_{i \leftarrow j}$  mappings as sub-matrices of  $A$  with respect to the appropriate  $(i, j)$  tracklet-detection pair:  $R_{i \leftarrow j} = A \left[ \sum_{i'=1}^{i-1} s_{i'} : \sum_{i'=1}^i s_{i'}, \sum_{j'=1}^{j-1} s_{j'} : \sum_{j'=1}^j s_{j'} \right]$ <sup>3</sup>. For a schematic representation of the procedure just described, see Figure 5.

RSM can be interpreted from an *attention* [67] perspective. The feature map of a tracklet  $t_i$  being reconstructed can be seen as a set of *queries*, and the “source” detection feature  $d_j$  can be interpreted both as *keys* and *values*. The goal is to compute the queries by linear combination of the values. The linear combination (attention) weights are computed using affinity between the queries and the keys. Specifically, we first compute a *global* affinity matrix between  $t_i$  and *all*  $d_{j'}$  for  $j' = 1, \dots, M$ , and then extract the corresponding sub-matrix for  $t_i$  and  $d_{j'}$  as the attention weights. Our formulation leads to a desired property: if the attention weights approach zero, the corresponding reconstructed point vectors will approach zero vectors, finally the RSM between  $t_i$  and  $d_j$  will approach zero.

Measuring similarity by reconstruction is popular in problems such as few-show learning [79], [96], self-supervised learning [42], and person re-identification [28]. However, reconstruction is typically framed as a ridge regression or optimal transport problem. RSM is more efficient than ridge regression (it has  $O(n^2)$  complexity in time, while ridge regression solvers usually have higher complexities), and it is computationally similar to calculate the Earth Moving Distance for the optimal transport problem. Appendix C shows a series of ablation studies illustrating the importance of the proposed RSM for the effectiveness of UniTrack on association type tasks.

### 3 Experiments

Task	SOT	VOS	MOT	MOTS	PoseTrack	PoseProp	VIS
Dataset	OTB 2015 [82]	DAVIS 2017 [54]	MOT 16 [47]	MOTS [69]	PoseTrack 2107 [1]	JHMDB [30]	YoutubeVIS [90]
Metrics	AUC	$\mathcal{J}$ -mean	IDF1 MOTA	IDF1 sMOTA	IDF1 MOTA ID-switch (IDs)	PCK	mAP

Table 1: List of datasets and metrics used to evaluate each task.

Since UniTrack does not require training of specific downstream tasks, we are able to effectively experiment with many alternative *base appearance models* (see Figure 3). Surprisingly, we find out that off-the-shelf features obtained from an ImageNet pretrained architecture outperform most of the appearance models we benchmarked, on most tasks. For this reason, in Section 3.1 we use it as default base appearance model within the UniTrack framework to compare against task-specific tracking methods. Then, in Section 3.2 we perform an extensive evaluation to benchmark a wide variety of modern self-supervised models, showing their strengths and weaknesses on all five tasks considered.

**Implementation details.** Unless specified, we adopt an ImageNet pre-trained ResNet-18 [27] as a default appearance model. To prevent excessive downsampling, we modify the spatial stride of layer3 and layer4 to 1, achieving a total stride of  $r = 8$ . We extract features from both layer3 and layer4. We report results with layer3 features when comparing against task-specific methods (Section 3.1), and with both layer3 and layer4 when evaluating multiple different representations (Section 3.2). Further implementation details are deferred to Appendix A and B.

**Datasets and evaluation metrics.** For fair comparison with existing methods, we report results on standard benchmarks with conventional metrics for each task. Table 1 summarizes the datasets (all publicly available) and evaluation metrics used in this work. In general, to compare with existing task-specific methods, we use the most popular benchmark for each task and report the standard metrics.

<sup>3</sup>Here we use a numpy-style matrix slicing notation to represent a submatrix, *i.e.*  $A[i:j, k:l]$  indicates a submatrix of  $A$  with row indices ranging from  $i$  to  $j$  and column indices ranging from  $k$  to  $l$ .

Methods	AUC↑	Methods	$\mathcal{J}$ -mean↑	Methods	IDF1↑	IDs↓	MOTA↑
<i>Supervised:</i>							
SiamFC [5]	58.2	SiamMask [74]	54.3	POI [94]	65.1	805	66.1
SiamRPN [36]	63.7	FEELVOS [68]	63.7	DeepSort-2 [80]	62.2	781	61.4
SiamRPN++ [35]	<b>69.6</b>	STM [51]	<b>79.2</b>	JDE [77]	55.8	1544	64.4
<i>Unsupervised:</i>							
UDT [71]	59.4	Colorization [70]	34.6	CTracker [53]	57.2	1897	67.6
UDT+ [71]	63.2	TimeCyclee [76]	40.1	TubeTK [52]	62.2	1236	66.9
LUDT [72]	60.2	UVC [39]	56.7	MAT [25]	63.8	928	73.5
LUDT+ [72]	<b>63.9</b>	CRW [29]	64.8	TraDes [81]	64.7	1144	70.1
UniTrack_XCorr	55.5	VFS [86]	<b>66.5</b>	CSTrack [40]	71.8	1071	70.7
UniTrack_DCF	61.8	UniTrack	58.4	FairMOT <sup>†</sup> [98]	<b>72.8</b>	1074	<b>74.9</b>
(a) SOT@OTB-2015 [82].							
(b) VOS@DAVIS-2017 [54].							
(c) MOT@MOT-16 [47] test split, private detection.							
Methods	IDF1↑	IDs↓	sMOTA↑	Methods	IDF1↑	IDs↓	MOTA↑
TrackRCNN [69]	42.4	567	40.6	MDPN [24]	-	-	50.6
SORTS [80]	57.3	577	55.0	OpenSVAI [50]	-	-	62.4
PointTrack [88]	42.9	868	62.3	Miracle [93]	-	-	64.0
GMPHD [60]	65.6	566	69.0	KeyTrack [59]	-	-	<b>66.6</b>
COSTA <sup>†</sup> [12]	<b>70.3</b>	<b>421</b>	<b>70.2</b>	LightTrack <sup>†</sup> [49]	52.2	<b>3024</b>	64.8
UniTrack <sup>†</sup>	67.2	622	68.9	UniTrack <sup>†</sup>	<b>73.2</b>	6760	63.5
(d) MOTS@MOTS [69] test split.							
(e) PoseTrack@PoseTrack2018 [1] val split.							

**Table 2:** Comparison with task-tailored unsupervised and supervised methods on five typical tracking tasks. <sup>†</sup> indicates methods using identical observations.

For association-type tasks (MOT, MOTS and PoseTrack), we first report the MOTA metric for its popularity and because it has been shown to highly correlate with qualitative perception of tracking accuracy [4]. However, the MOTA metric disproportionately overweights detection accuracy [45], [66] over identity preservation within tracks, which for many applications is vital. For this reason, we also report identity based metrics such as IDF-1 and ID-switch. We also adopt the recently-introduced HOTA [45] to capture the overall tracking accuracy when comparing self-supervised methods.

For pose tracking, results are averaged for IDF-1 and MOTA, and summed for ID-switch, over 15 key points. In the main text, we only report results for the first five tasks from Table 1, while for the remaining two (PoseProp and VIS) we provide additional results in Appendix D.

### 3.1 Comparison with task-specific tracking methods

**Unsupervised methods.** We observe that UniTrack performs favourably against unsupervised state-of-the-art methods in both the propagation-type tasks we considered (Table 2a and 2b). For SOT, UniTrack with a DCF head [73] outperforms UDT [71] (a strong recent method) by 2.4 AUC percentage points, while it is surpassed by LUDT+ [72] by 2.1 points. Considering that LUDT+ adopts an additional online template update mechanism [13] while ours does not, we believe the gap could be closed. In VOS, existing unsupervised methods are usually trained on video datasets [29], [39], [86]. Nonetheless, results show that even if our appearance model is pre-trained on still images, its tracking accuracy is still competitive. Note that, for association-type tasks, we are not aware of any existing unsupervised learning method, and thus in this case we limit the comparison to supervised methods.

**Comparison with supervised methods.** In general, UniTrack with a ResNet-18 appearance model already performs on par with several existing task-specific supervised methods, and in several tasks it even shows superior accuracy, especially for identity-related metrics. (1) For SOT, UniTrack with a DCF head outperforms SiamFC [5] by 3.6 AUC points. This is a significant margin considering that SiamFC is trained with a large amount of crops from video datasets with annotated bounding boxes. (2) For VOS, UniTrack surpasses SiamMask [74] by 4.1  $\mathcal{J}$ -mean points, despite this being trained on the joint set of three large-scale video datasets [15], [41], [87]. (3) For MOT, we employ the same detections used by the state-of-the-art tracker FairMOT [98]. The appearance embedding in FairMOT is trained with 270K bounding boxes of 8.7K labeled identities, from a MOT-specific dataset. In contrast, despite our appearance model not being trained with any MOT-specific data, our IDF1 score is quite competitive (71.8 v.s. 72.8 of FairMOT), and the ID switches are considerably reduced by 36.4%, from 1074 to 683. (4) For MOTS, we start from the same

Representation	SOT [82]		VOS [54]		MOT [47]		MOTS [69]		PoseTrack [1]	
	AUC <sub>Xcorr</sub> ↑	AUC <sub>DCF</sub> ↑	$\mathcal{J}$ -mean↑	IDF1↑	HOTA↑	IDF1↑	HOTA↑	IDF1↑	IDs↓	
Rand. Init.	<b>10.3</b> / 9.0	<b>28.0</b> / 20.0	29.3 / <b>33.9</b>	8.4 / <b>8.9</b>	8.4 / <b>8.5</b>	20.8 / <b>23.1</b>	25.9 / <b>28.7</b>	<b>40.2</b> / 38.5	<b>88792</b> / 90963	
Supervised	<b>58.6</b> / 49.5	<b>62.0</b> / 53.9	<b>62.3</b> / 57.9	<b>75.6</b> / 73.2	<b>63.3</b> / 61.8	68.4 / <b>69.4</b>	<b>70.2</b> / <b>71.0</b>	73.7 / 73.3	<b>6969</b> / 7103	
InsDis [83]	<b>47.6</b> / 47.3	<b>61.8</b> / 51.1	<b>62.6</b> / 60.1	66.7 / <b>73.9</b>	57.9 / <b>61.9</b>	<b>68.4</b> / 68.0	69.6 / <b>70.3</b>	72.4 / <b>73.9</b>	7106 / <b>7015</b>	
MoCoV1 [26]	<b>50.9</b> / 47.9	<b>62.2</b> / 53.7	<b>61.5</b> / 57.9	69.2 / <b>74.1</b>	59.4 / <b>61.9</b>	<b>70.6</b> / 69.3	<b>71.6</b> / 70.9	72.8 / <b>73.9</b>	<b>6872</b> / 7092	
PCLV1 [37]	<b>56.8</b> / 31.5	61.3 / 35.0	60.4 / 38.8	<b>74.8</b> / 68.8	<b>62.8</b> / 59.1	<b>67.6</b> / 65.2	69.7 / 67.3	73.3 / 71.1	<b>6855</b> / 10694	
PIRL [48]	43.8 / <b>51.0</b>	<b>61.2</b> / 53.4	<b>60.8</b> / 57.7	62.0 / <b>73.4</b>	54.6 / <b>61.9</b>	66.0 / <b>67.4</b>	66.7 / <b>69.9</b>	72.1 / <b>73.0</b>	7235 / <b>7173</b>	
PCLV2 [37]	<b>54.9</b> / 50.3	<b>62.5</b> / 51.6	<b>61.2</b> / 52.5	<b>74.9</b> / 72.9	<b>62.7</b> / 61.8	<b>68.3</b> / 66.6	<b>70.5</b> / 69.0	73.5 / 73.4	<b>6859</b> / 8489	
SimCLRv1 [9]	47.3 / <b>51.9</b>	61.3 / 50.7	60.5 / 56.5	<b>66.9</b> / <b>75.6</b>	<b>57.7</b> / <b>63.2</b>	65.8 / <b>67.6</b>	67.7 / <b>69.5</b>	72.3 / 73.5	7084 / 7367	
MoCoV2 [11]	<b>53.7</b> / 47.2	61.5 / 53.3	61.2 / 54.0	72.0 / <b>74.9</b>	61.2 / <b>62.8</b>	67.5 / 67.3	<b>69.6</b> / <b>69.6</b>	73.0 / 73.7	<b>6932</b> / 7702	
SimCLRv2 [10]	50.0 / <b>54.7</b>	<b>61.7</b> / 56.8	<b>61.6</b> / 58.4	<b>67.6</b> / <b>75.7</b>	58.1 / <b>63.3</b>	<b>69.1</b> / 67.4	<b>70.4</b> / 69.4	72.5 / <b>73.6</b>	7228 / 7856	
SeLaV2 [2]	<b>51.0</b> / 9.6	<b>63.1</b> / 14.2	60.2 / 40.2	68.8 / <b>68.9</b>	59.0 / 59.3	66.8 / 66.1	<b>68.7</b> / 68.5	<b>72.9</b> / 72.3	6983 / 7815	
Infomin [64]	<b>48.5</b> / 46.8	61.2 / 51.9	<b>58.4</b> / 51.1	66.7 / 73.4	57.6 / <b>61.9</b>	66.7 / 66.3	68.5 / <b>68.8</b>	<b>72.5</b> / <b>74.0</b>	7066 / 7901	
BarLowTwins [95]	<b>44.5</b> / <b>55.5</b>	60.5 / 60.1	<b>61.7</b> / <b>57.8</b>	63.7 / <b>74.5</b>	55.4 / <b>62.4</b>	<b>68.7</b> / 67.4	69.5 / <b>69.8</b>	72.3 / <b>74.3</b>	7131 / 7456	
BYOL [23]	<b>48.3</b> / <b>55.5</b>	58.9 / 56.8	<b>58.8</b> / 54.3	65.3 / <b>74.9</b>	56.8 / <b>62.9</b>	<b>70.1</b> / 66.8	<b>70.8</b> / 69.3	72.4 / <b>73.8</b>	7213 / 8032	
DeepClusterV2 [7]	51.5 / <b>52.9</b>	<b>61.2</b> / <b>61.2</b>	<b>59.3</b> / 53.4	66.9 / <b>75.1</b>	<b>57.8</b> / <b>63.5</b>	67.7 / 67.4	69.4 / <b>69.8</b>	72.7 / <b>73.7</b>	7018 / 7283	
SwAV [8]	49.2 / 52.4	<b>61.5</b> / 59.4	<b>59.4</b> / 57.0	65.6 / <b>74.4</b>	56.9 / <b>62.3</b>	<b>68.8</b> / 67.0	<b>69.9</b> / 69.5	72.7 / <b>73.6</b>	7025 / 7377	
PixPro [85]	40.5 / <b>49.2</b>	57.4 / 49.3	<b>56.4</b> / 52.2	61.7 / <b>67.7</b>	54.3 / <b>58.6</b>	64.2 / <b>66.2</b>	65.1 / <b>67.6</b>	72.4 / <b>73.1</b>	7163 / <b>6953</b>	
DetCo [84]	<b>55.0</b> / 47.1	59.0 / 53.2	<b>62.3</b> / 56.1	<b>75.3</b> / 72.9	<b>62.8</b> / 61.6	<b>67.8</b> / 66.8	<b>70.0</b> / 69.4	<b>73.9</b> / 73.3	7357 / 8009	
TimeCycle [76]	43.8 / 24.2	57.5 / 48.7	51.8 / 48.9	68.7 / 28.2	59.3 / 25.5	<b>69.9</b> / 47.1	71.3 / 49.3	72.0 / 62.3	7837 / 27884	

**Table 3:** Tracking performance of pre-trained *image-based* SSL models. All methods use a ResNet-50 backbone. For each cell, we report the results obtained from features at [layer3 / layer4], and the best performance between the two is **bolded**. We then use the best of the two to rank the models in each column, and visualize better performance with darker shades of red. For each column, the best overall result is underlined.

Representation	SOT [82]		VOS [54]		MOT [47]		MOTS [69]		PoseTrack [1]	
	AUC <sub>Xcorr</sub> ↑	AUC <sub>DCF</sub> ↑	$\mathcal{J}$ -mean↑	IDF1↑	HOTA↑	IDF1↑	HOTA↑	IDF1↑	IDs↓	
Rand. Init.	16.0 / <b>18.2</b>	<b>36.1</b> / 32.1	33.0 / <b>36.7</b>	<b>18.4</b> / 14.6	<b>20.2</b> / 12.9	<b>34.5</b> / 33.1	<b>39.9</b> / 37.6	<b>52.8</b> / 50.5	<b>65317</b> / 66230	
Supervised	<b>55.0</b> / 46.2	<b>61.8</b> / 52.6	<b>58.4</b> / 46.7	<b>74.8</b> / 74.5	<b>62.7</b> / 62.1	67.6 / <b>68.6</b>	69.8 / <b>70.5</b>	72.7 / <b>73.2</b>	6808 / 7024	
Color. [70]+mem.	41.6 / <b>43.4</b>	56.7 / <b>58.7</b>	<b>53.6</b> / <b>59.7</b>	<b>64.9</b> / 62.8	<b>56.8</b> / 55.5	<b>68.8</b> / 66.1	<b>69.4</b> / 66.3	72.4 / <b>72.6</b>	6850 / <b>6778</b>	
UVC [39]	<b>46.0</b> / 38.7	58.1 / <b>59.9</b>	<b>56.5</b> / 53.9	<b>66.9</b> / 64.5	<b>57.7</b> / 54.1	<b>69.9</b> / 68.7	<b>69.6</b> / 69.4	72.6 / <b>72.8</b>	6843 / 6972	
CRW [29]	<b>46.3</b> / <b>49.1</b>	<b>58.9</b> / 54.9	<b>63.2</b> / 60.7	67.8 / <b>73.0</b>	58.4 / <b>61.7</b>	69.0 / <b>71.3</b>	69.2 / <b>71.9</b>	72.7 / <b>73.0</b>	6799 / <b>6761</b>	

**Table 4:** Tracking performance of pre-trained *video-based* SSL models. All methods use a ResNet-18 backbone.

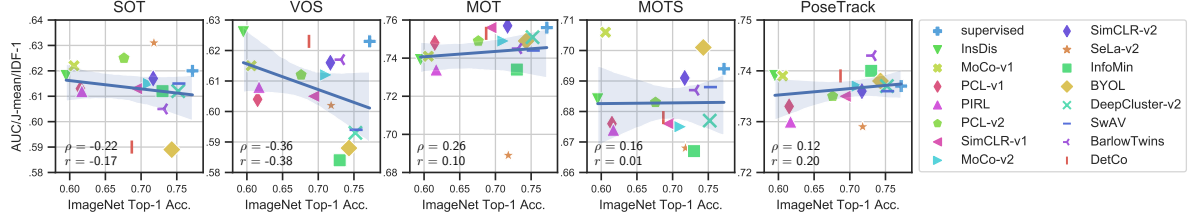


**Figure 6:** Tracking performance is poorly correlated with ImageNet accuracy. On the x-axes we plot ImageNet linear probe top-1 accuracy and on the y-axes the performance on five tracking tasks. Correlation coefficients (Spearman’s  $\rho$  and Pearson’s  $r$ ) are shown in the left bottom of each plot. Analysis inspired by [18]

segmentation masks used by the COSTA [12] tracker, and observe a degradation in terms of ID switches (622 vs the 421 of the state of the art), and also a gap in IDF1 and sMOTA. (5) Finally, for pose tracking, we employ the same pose estimator used by LightTrack [49]. Compared with LightTrack, the MOTA of UniTrack degrades of 1.3 points because of an increased amount of ID switches. However, the IDF-1 score is improved by a significant margin (+21.0 points). This shows UniTrack preserves identity more accurately for long tracklets: Even if ID switches occur more frequently, after a short period UniTrack is able to correct the wrong association, therefore IDF-1 is much higher.

### 3.2 UniTrack as evaluation platform of previously-learned representations

The process of evaluating representations learned via self-supervised learning (SSL) often involves additional training [9], [18], [26], for instance via the use of *linear probes* [97]: Fix the pre-trained model and train an additional linear classifier on top of the model, and then evaluate classification performance. In contrast, using UniTrack as evaluation platform (1) does not require any additional training and (2) enables the evaluation on a battery of important video tasks, which

have generally been neglected in self-supervised-learning papers in favour of more established image-level tasks such as classification.

In this section, we evaluate three types of SSL representations: **(a)** Image-level representations learned from images, *e.g.* MoCo [26] and BYOL [23]; **(b)** Pixel-level representations learned from images (such as DetCo [84] and PixPro [85]) and **(c)** videos (such as UVC [39] and CRW [29]). For all methods considered, we use the pre-trained weights provided by the authors.

Results are shown in Table 3 and 4, where we report the results obtained by using features both at `layer3` and `layer4` of the pre-trained backbone (separated by a ‘/’ in the table). Note that, for this analysis only, for association-type tasks motion cues are discarded to better highlight distinctions between different representations and avoid potential confounding factors. Figure 1 provides a high-level summary of the results by focusing on the ranking obtained by different SSL methods on the five tasks considered (each represented by a vertex in the radar-style plot). Several observations can be made:

**(1)** *There is no significant correlation between “linear probe accuracy” on ImageNet and overall tracking performance.* The linear probe approach [97] has become a standard way to compare SSL representations. In Figure 6, we plot tracking performance on five tasks (y-axes) against ImageNet top-1 accuracy of 16 different models (x-axes), and report Pearson and Spearman (rank) correlation coefficients. We observe that the correlation between ImageNet accuracy and tracking performance is small, *i.e.* the Pearson’s  $r$  ranges from  $-0.38$  to  $+0.20$ , and Spearman’s  $\rho$  ranges from  $-0.36$  to  $+0.26$ . For most tasks, there is almost no correlation, while for VOS the two measures are mildly *inversely* correlated. The result suggests that evaluating SSL models on five extra tasks with UniTrack could constitute a useful complement to ImageNet linear probe evaluation, and encourage the SSL community to pursue the design of even more *general purpose* representations.

**(2)** *A vanilla ImageNet-trained supervised representation is surprisingly effective across the board.* On most tasks, it reports a performance that is on par with the best representation for that task. This is particularly evident from Figure 1, where its performance is outlined as a gray dashed line. This result suggests that results obtained with vanilla ImageNet features should be reported when investigating new tracking methods.

**(3)** *No SSL representation dominates all tasks.* Recently, it has been shown how SSL-trained representations can match or surpass their supervised counterparts on ImageNet classification (*e.g.* [23]) and many downstream tasks [18], [84]. Similarly, within UniTrack the best SSL representation always outperforms or matches the vanilla supervised representation on every single task. However, no individual SSL representation is able to beat the vanilla ImageNet-trained representation on every task. Among SSL methods, two emerge as clear “winners” from this comparison. One is SimCLR-v2 [10], which performs almost as well as the vanilla ImageNet-trained representation on three tasks and outperforms it on MOT. The other is MoCo [26], which despite being one of the worst methods on MOT, is able to outperform the vanilla ImageNet-trained representation on SOT, MOTS and PoseTrack. Curiously, MoCo-v2 [11] has an overall worse performance than its predecessor.

**(4)** *Pixel-level SSL representations do not seem to have a consistent advantage in pixel-level tasks.* In Table 4 and at the bottom of Table 3 we compare recent SSL representations trained with pixel-level proxy tasks: PixPro [85], DetCo [84], TimeCycle [76], Colorization [70], UVC [39] and Contrastive Random Walk (CRW) [29]. Considering that pixel-level models leverage more fine-grained information during training, one may expect them to outperform image-based models in the tracking tasks where this is important. It is not straightforward to compare pixel-level SSL models with image-level ones, as the two types employ different default backbone networks. However, note how good image-based models (MoCo-v1, SimCLR-v2) are on par with their supervised counterpart in all tasks, while good pixel-level models (DetCo, CRW) still have gaps with respect to their supervised counterparts in tasks like SOT and MOT. Moreover, from Table 3, one can notice how the last three rows, despite representing methods leveraging pixel-level information during training, are actually outperformed by image-level representations on the pixel-level tasks of VOS, MOTS and PoseTrack.

**(5)** *SSL representations trained from video data do not seem to present a consistent advantage over those trained from images.* Beside being trained with pixel-level proxy tasks, TimeCycle [76], Colorization [70], UVC [39] and CRW [29] are also trained on large video datasets, which should intuitively provide an advantage for video-based tasks like the five considered in this paper. Instead, with the exception of CRW [29] (which is the best-performing method for VOS and MOTS), they are generally outperformed by ImageNet-trained features.

## 4 Related Work

**Sharing appearance model across multiple tracking tasks** has not yet being extensively studied in literature, especially not in the context of SSL representations. Some existing methods do share a common architecture across tasks.

For instance, STEm-Seg [3] addresses VIS [90] and MOTS; while TraDeS [81] addresses 2D/3D MOT, MOTS and VIS. However, both methods train their models separately and on different datasets for every task. Conversely, we reuse the *same* previously-learned representation across five tasks and we do not require any additional training. A promising direction for future work would be to use UniTrack to train a shared representation in a multi-task fashion. To our knowledge, only a few approaches do adopt a multi-task strategy [46], [74], [99], and they usually consider SOT and VOS tasks only. In general, despite the multi-task direction being surely interesting, it requires the availability of large-scale datasets with annotations in multiple formats, and costly training. These are two of the main reasons for which we believe that having a framework that allows to achieve competitive performance on multiple tasks with previously-trained models is a worthwhile endeavour.

**Self-supervised model evaluation.** Given the difference between the pretext tasks used to train self-supervised models and the downstream tasks used to evaluate them, the comparison between self-supervised approaches has always been a delicate matter. Existing evaluation strategies typically require additional training once a general-purpose representation has been obtained. One strategy keeps the representation fixed, and then trains additional task-specific heads with very limited capacity (*e.g.* a linear classifier [9], [22], [26] for image recognition or classification/regression heads for object detection [22]). A second strategy, instead, leverages SSL to obtain particularly effective initializations, and then proceeds to fine-tune such initialized models on the downstream task of interest. A wider range of tasks can be tested using this setup, such as semantic segmentation [18], [22] and surface normal estimation [22], [75]. In contrast, UniTrack provides a simpler way to evaluate SSL models, one that does not require additional training or fine-tuning. Also, this work is the first to extend SSL evaluation to a set of diverse video tasks. We believe this contribution will allow the study of self-supervised method with a broader scope of applicability. Our work is also related to a line of self-supervised learning methods [29], [34], [39], [70] that learn their representations in a task-agnostic fashion, and then test it on *propagation* tasks (SOT and VOS). The design of UniTrack is inspired by their task-agnostic philosophy, while significantly extending their scope to a new set of tasks.

Finally, the recent work and the visualizations of Ericsson *et al.* [18] have been instrumental to inspire the analysis between SSL methods of Section 3.2, and Figure 1 and 6. Different to them, we focus exclusively on video tasks.

## 5 Conclusion

Do different tracking tasks require different appearance models? In order to address this question, the proposed UniTrack framework has been instrumental, as it has allowed to easily experiment with alternative representations on a wide variety of downstream problems. From our study, the answer is negative: it turns out that a *single shared* appearance model can perform competitively against dedicated methods, without any training. Our findings point towards the existence of several strong baselines which should be carefully considered when designing task-specific approaches. Moreover, our work also allows to significantly extend the evaluation of self-supervised models to five new tasks that, as we demonstrated in our experiments, have little correlation with the standard linear-probe approach, and thus high informative value. We believe this will encourage the community to develop self-supervised representations that are of “general purpose” in a broader sense.

## References

- [1] Mykhaylo Andriluka, Umar Iqbal, Eldar Insafutdinov, et al. “Posetrack: A benchmark for human pose estimation and tracking”. In: *CVPR*. 2018.
- [2] Yuki Markus Asano, Christian Rupprecht, and Andrea Vedaldi. “Self-labelling via simultaneous clustering and representation learning”. In: *ICLR*. 2020.
- [3] Ali Athar, Sabarinath Mahadevan, Aljoša Ošep, et al. “STEM-Seg: Spatio-temporal Embeddings for Instance Segmentation in Videos”. In: *ECCV*. 2020.
- [4] Keni Bernardin and Rainer Stiefelhagen. “Evaluating multiple object tracking performance: the clear mot metrics”. In: *EURASIP Journal on Image and Video Processing* 2008 (2008), pp. 1–10.
- [5] Luca Bertinetto, Jack Valmadre, Joao F Henriques, et al. “Fully-convolutional siamese networks for object tracking”. In: *ECCV workshops*. 2016.
- [6] Jiale Cao, Rao Muhammad Anwer, Hisham Cholakkal, et al. “SipMask: Spatial Information Preservation for Fast Image and Video Instance Segmentation”. In: *ECCV*. 2020.
- [7] Mathilde Caron, Piotr Bojanowski, Armand Joulin, et al. “Deep clustering for unsupervised learning of visual features”. In: *ECCV*. 2018.
- [8] Mathilde Caron, Ishan Misra, Julien Mairal, et al. “Unsupervised learning of visual features by contrasting cluster assignments”. In: *NeurIPS*. 2018.
- [9] Ting Chen, Simon Kornblith, Mohammad Norouzi, et al. “A simple framework for contrastive learning of visual representations”. In: *ICML*. 2020.
- [10] Ting Chen, Simon Kornblith, Kevin Swersky, et al. “Big Self-Supervised Models are Strong Semi-Supervised Learners”. In: *arXiv:2006.10029*. 2020.
- [11] Xinlei Chen, Haoqi Fan, Ross Girshick, et al. “Improved baselines with momentum contrastive learning”. In: *arXiv:2003.04297*. 2020.
- [12] *COSTA\_st tracker*. <https://motchallenge.net/method/MOTS=87&chl=17>.
- [13] Martin Danelljan, Goutam Bhat, Fahad Shahbaz Khan, et al. “Eco: Efficient convolution operators for tracking”. In: *CVPR*. 2017.
- [14] Patrick Dendorfer, Hamid Rezatofighi, Anton Milan, et al. “Mot20: A benchmark for multi object tracking in crowded scenes”. In: *arXiv:2003.09003*. 2020.
- [15] Jia Deng, Wei Dong, Richard Socher, et al. “Imagenet: A large-scale hierarchical image database”. In: *CVPR*. 2009.
- [16] Jacob Devlin, Ming-Wei Chang, Kenton Lee, et al. “Bert: Pre-training of deep bidirectional transformers for language understanding”. In: *NAACL*. 2018.
- [17] Alexey Dosovitskiy, Philipp Fischer, Eddy Ilg, et al. “Flownet: Learning optical flow with convolutional networks”. In: *ICCV*. 2015.
- [18] Linus Ericsson, Henry Gouk, and Timothy M Hospedales. “How Well Do Self-Supervised Models Transfer?” In: *CVPR*. 2021.
- [19] Mark Everingham, Luc Van Gool, Christopher KI Williams, et al. “The pascal visual object classes (voc) challenge”. In: *International journal of computer vision* 88.2 (2010), pp. 303–338.
- [20] Masoud Faraki, Xiang Yu, Yi-Hsuan Tsai, et al. “Cross-Domain Similarity Learning for Face Recognition in Unseen Domains”. In: *arXiv:2103.07503*. 2021.
- [21] Pedro F Felzenszwalb, Ross B Girshick, and David McAllester. “Cascade object detection with deformable part models”. In: *CVPR*. 2010.
- [22] Priya Goyal, Dhruv Mahajan, Abhinav Gupta, et al. “Scaling and Benchmarking Self-Supervised Visual Representation Learning”. In: *arXiv:1905.01235*. 2019.
- [23] Jean-Bastien Grill, Florian Strub, Florent Altché, et al. “Bootstrap your own latent: A new approach to self-supervised learning”. In: *NeurIPS*. 2020.
- [24] Hengkai Guo, Tang Tang, Guozhong Luo, et al. “Multi-domain pose network for multi-person pose estimation and tracking”. In: *ECCV workshop*. 2018.
- [25] Shoudong Han, Piao Huang, Hongwei Wang, et al. “MAT: Motion-Aware Multi-Object Tracking”. In: *arXiv:2009.04794*. 2020.
- [26] Kaiming He, Haoqi Fan, Yuxin Wu, et al. “Momentum contrast for unsupervised visual representation learning”. In: *CVPR*. 2020.
- [27] Kaiming He, Xiangyu Zhang, Shaoqing Ren, et al. “Deep residual learning for image recognition”. In: *CVPR*. 2016.

[28] Lingxiao He, Jian Liang, Haiqing Li, et al. “Deep spatial feature reconstruction for partial person re-identification: Alignment-free approach”. In: *CVPR*. 2018.

[29] Allan Jabri, Andrew Owens, and Alexei A Efros. “Space-time correspondence as a contrastive random walk”. In: *NeurIPS*. 2020.

[30] H. Jhuang, J. Gall, S. Zuffi, et al. “Towards understanding action recognition”. In: *ICCV*. 2013.

[31] Rudolph Emil Kalman. “A new approach to linear filtering and prediction problems”. In: (1960).

[32] Matej Kristan, Jiri Matas, Aleš Leonardis, et al. “A novel performance evaluation methodology for single-target trackers”. In: *IEEE TPAMI* (2016).

[33] Harold W Kuhn. “The Hungarian method for the assignment problem”. In: *Naval research logistics quarterly* 2.1-2 (1955), pp. 83–97.

[34] Zihang Lai, Erika Lu, and Weidi Xie. “MAST: A memory-augmented self-supervised tracker”. In: *CVPR*. 2020.

[35] Bo Li, Wei Wu, Qiang Wang, et al. “Siamrpn++: Evolution of siamese visual tracking with very deep networks”. In: *CVPR*. 2019.

[36] Bo Li, Junjie Yan, Wei Wu, et al. “High performance visual tracking with siamese region proposal network”. In: *CVPR*. 2018.

[37] Junnan Li, Pan Zhou, Caiming Xiong, et al. “Prototypical contrastive learning of unsupervised representations”. In: *ICLR*. 2021.

[38] Wei Li, Rui Zhao, Tong Xiao, et al. “Deepreid: Deep filter pairing neural network for person re-identification”. In: *CVPR*. 2014.

[39] Xueting Li, Sifei Liu, Shalini De Mello, et al. “Joint-task self-supervised learning for temporal correspondence”. In: *NeurIPS*. 2019.

[40] Chao Liang, Zhipeng Zhang, Yi Lu, et al. “Rethinking the competition between detection and ReID in Multi-Object Tracking”. In: *arXiv:2010.12138*. 2020.

[41] Tsung-Yi Lin, Michael Maire, Serge Belongie, et al. “Microsoft coco: Common objects in context”. In: *ECCV*. 2014.

[42] Songtao Liu, Zeming Li, and Jian Sun. “Self-EMD: Self-Supervised Object Detection without ImageNet”. In: *arXiv:2011.13677*. 2020.

[43] Chen Long, Ai Haizhou, Zhuang Zijie, et al. “Real-time Multiple People Tracking with Deeply Learned Candidate Selection and Person Re-identification”. In: *ICME*. 2018.

[44] Jonathan Long, Ning Zhang, and Trevor Darrell. “Do convnets learn correspondence?” In: *NeurIPS*. 2014.

[45] Jonathon Luiten, Aljosa Osep, Patrick Dendorfer, et al. “HOTA: A Higher Order Metric for Evaluating Multi-Object Tracking”. In: *IJCV* (2020).

[46] Alan Lukezic, Jiri Matas, and Matej Kristan. “D3S-A discriminative single shot segmentation tracker”. In: *CVPR*. 2020.

[47] Anton Milan, Laura Leal-Taixé, Ian Reid, et al. “MOT16: A benchmark for multi-object tracking”. In: *arXiv:1603.00831*. 2016.

[48] Ishan Misra and Laurens van der Maaten. “Self-supervised learning of pretext-invariant representations”. In: *CVPR*. 2020.

[49] Guanghan Ning and Heng Huang. “LightTrack: A Generic Framework for Online Top-Down Human Pose Tracking”. In: *CVPR, workshop*. 2020.

[50] Guanghan Ning, Ping Liu, Xiaochuan Fan, et al. “A top-down approach to articulated human pose estimation and tracking”. In: *ECCV, workshop*. 2018.

[51] Seoung Wug Oh, Joon-Young Lee, Ning Xu, et al. “Video object segmentation using space-time memory networks”. In: *ICCV*. 2019.

[52] Bo Pang, Yizhuo Li, Yifan Zhang, et al. “TubeTK: Adopting tubes to track multi-object in a one-step training model”. In: *CVPR*. 2020.

[53] Jinlong Peng, Changan Wang, Fangbin Wan, et al. “Chained-tracker: Chaining paired attentive regression results for end-to-end joint multiple-object detection and tracking”. In: *ECCV*. 2020.

[54] F. Perazzi, J. Pont-Tuset, B. McWilliams, et al. “A Benchmark Dataset and Evaluation Methodology for Video Object Segmentation”. In: *CVPR*. 2016.

[55] Shaoqing Ren, Kaiming He, Ross Girshick, et al. “Faster r-cnn: Towards real-time object detection with region proposal networks”. In: *ICCV*. 2015.

[56] Ergys Ristani, Francesco Solera, Roger Zou, et al. “Performance measures and a data set for multi-target, multi-camera tracking”. In: *ECCV*. 2016.

[57] Ergys Ristani and Carlo Tomasi. “Features for multi-target multi-camera tracking and re-identification”. In: *CVPR*. 2018.

[58] Nathan Silberman, Derek Hoiem, Pushmeet Kohli, et al. “Indoor segmentation and support inference from rgbd images”. In: *ECCV*. 2012.

[59] Michael Snower, Asim Kadav, Farley Lai, et al. “15 Keypoints Is All You Need”. In: *CVPR*. 2020.

[60] Young-min Song and Moongu Jeon. “Online Multi-Object Tracking and Segmentation with GMPHD Filter and Simple Affinity Fusion”. In: *arXiv:2009.00100*. 2020.

[61] Yifan Sun, Qin Xu, Yali Li, et al. “Perceive where to focus: Learning visibility-aware part-level features for partial person re-identification”. In: *CVPR*. 2019.

[62] Yifan Sun, Liang Zheng, Yi Yang, et al. “Beyond part models: Person retrieval with refined part pooling (and a strong convolutional baseline)”. In: *ECCV*. 2018.

[63] Siyu Tang, Mykhaylo Andriluka, Bjoern Andres, et al. “Multiple people tracking by lifted multicut and person re-identification”. In: *CVPR*. 2017.

[64] Yonglong Tian, Chen Sun, Ben Poole, et al. “What makes for good views for contrastive learning”. In: *NeurIPS*. 2020.

[65] Jack Valmadre, Luca Bertinetto, Joao Henriques, et al. “End-to-end representation learning for correlation filter based tracking”. In: *CVPR*. 2017.

[66] Jack Valmadre, Alex Bewley, Jonathan Huang, et al. “Local Metrics for Multi-Object Tracking”. In: *arXiv preprint arXiv:2104.02631* (2021).

[67] Ashish Vaswani, Noam Shazeer, Niki Parmar, et al. “Attention is All you Need”. In: *NeurIPS*. 2017.

[68] Paul Voigtlaender, Yuning Chai, Florian Schroff, et al. “Feelvos: Fast end-to-end embedding learning for video object segmentation”. In: *CVPR*. 2019.

[69] Paul Voigtlaender, Michael Krause, Aljosa Osep, et al. “Mots: Multi-object tracking and segmentation”. In: *CVPR*. 2019.

[70] Carl Vondrick, Abhinav Shrivastava, Alireza Fathi, et al. “Tracking emerges by colorizing videos”. In: *ECCV*. 2018.

[71] Ning Wang, Yibing Song, Chao Ma, et al. “Unsupervised Deep Tracking”. In: *CVPR*. 2019.

[72] Ning Wang, Wengang Zhou, Yibing Song, et al. “Unsupervised deep representation learning for real-time tracking”. In: *IJCV* (2020).

[73] Qiang Wang, Jin Gao, Junliang Xing, et al. “Dcfnet: Discriminant correlation filters network for visual tracking”. In: *arXiv:1704.04057*. 2017.

[74] Qiang Wang, Li Zhang, Luca Bertinetto, et al. “Fast online object tracking and segmentation: A unifying approach”. In: *CVPR*. 2019.

[75] Xiaolong Wang and Abhinav Gupta. “Unsupervised learning of visual representations using videos”. In: *ICCV*. 2015.

[76] Xiaolong Wang, Allan Jabri, and Alexei A Efros. “Learning correspondence from the cycle-consistency of time”. In: *CVPR*. 2019.

[77] Zhongdao Wang, Liang Zheng, Yixuan Liu, et al. “Towards real-time multi-object tracking”. In: *ECCV*. 2020.

[78] Shih-En Wei, Varun Ramakrishna, Takeo Kanade, et al. “Convolutional pose machines”. In: *CVPR*. 2016.

[79] Davis Wertheimer, Luming Tang, and Bharath Hariharan. “Fine-Grained Few-Shot Classification with Feature Map Reconstruction Networks”. In: *CVPR*. 2021.

[80] Nicolai Wojke, Alex Bewley, and Dietrich Paulus. “Simple online and realtime tracking with a deep association metric”. In: *ICIP*. 2017.

[81] Jialian Wu, Jiale Cao, Liangchen Song, et al. “Track to Detect and Segment: An Online Multi-Object Tracker”. In: *CVPR*. 2021.

[82] Yi Wu, Jongwoo Lim, and Ming-Hsuan Yang. “Online object tracking: A benchmark”. In: *CVPR*. 2013.

[83] Zhirong Wu, Yuanjun Xiong, Stella X Yu, et al. “Unsupervised feature learning via non-parametric instance discrimination”. In: *CVPR*. 2018.

[84] Enze Xie, Jian Ding, Wenhui Wang, et al. “DetCo: Unsupervised Contrastive Learning for Object Detection”. In: *arXiv:2102.04803*. 2021.

[85] Zhenda Xie, Yutong Lin, Zheng Zhang, et al. “Propagate Yourself: Exploring Pixel-Level Consistency for Unsupervised Visual Representation Learning”. In: *CVPR*. 2021.

[86] Jiarui Xu and Xiaolong Wang. “Rethinking Self-supervised Correspondence Learning: A Video Frame-level Similarity Perspective”. In: *arXiv:2103.17263*. 2021.

[87] Ning Xu, Linjie Yang, Yuchen Fan, et al. “Youtube-vos: Sequence-to-sequence video object segmentation”. In: *ECCV*. 2018.

[88] Zhenbo Xu, Wei Zhang, Xiao Tan, et al. “Segment as points for efficient online multi-object tracking and segmentation”. In: *ECCV*. 2020.

[89] Fan Yang, Wongun Choi, and Yuanqing Lin. “Exploit all the layers: Fast and accurate cnn object detector with scale dependent pooling and cascaded rejection classifiers”. In: *CVPR*. 2016.

[90] Linjie Yang, Yuchen Fan, and Ning Xu. “Video instance segmentation”. In: *ICCV*. 2019.

[91] Linjie Yang, Yanran Wang, Xuehan Xiong, et al. “Efficient video object segmentation via network modulation”. In: *CVPR*. 2018.

[92] Linjie Yang, Yanran Wang, Xuehan Xiong, et al. “Efficient video object segmentation via network modulation”. In: *CVPR*. 2018.

[93] Dongdong Yu, Kai Su, Jia Sun, et al. “Multi-person pose estimation for pose tracking with enhanced cascaded pyramid network”. In: *ECCV workshop*. 2018.

[94] Fengwei Yu, Wenbo Li, Quanquan Li, et al. “Poi: Multiple object tracking with high performance detection and appearance feature”. In: *ECCV workshop*. 2016.

[95] Jure Zbontar, Li Jing, Ishan Misra, et al. “Barlow Twins: Self-Supervised Learning via Redundancy Reduction”. In: *arXiv:2103.03230*. 2021.

[96] Chi Zhang, Yujun Cai, Guosheng Lin, et al. “DeepEMD: Few-Shot Image Classification With Differentiable Earth Mover’s Distance and Structured Classifiers”. In: *CVPR*. 2020.

[97] Richard Zhang, Phillip Isola, and Alexei A Efros. “Split-brain autoencoders: Unsupervised learning by cross-channel prediction”. In: *CVPR*. 2017.

[98] Yifu Zhang, Chunyu Wang, Xinggang Wang, et al. “FairMOT: On the Fairness of Detection and Re-Identification in Multiple Object Tracking”. In: *arXiv:2004.01888*. 2020.

[99] Zhipeng Zhang, Bing Li, Weiming Hu, et al. “Towards Accurate Pixel-wise Object Tracking by Attention Retrieval”. In: *arXiv:2008.02745*. 2020.

[100] Liang Zheng, Liyue Shen, Lu Tian, et al. “Scalable person re-identification: A benchmark”. In: *ICCV*. 2015.

[101] Bolei Zhou, Hang Zhao, Xavier Puig, et al. “Scene parsing through ade20k dataset”. In: *CVPR*. 2017.

[102] Xingyi Zhou, Vladlen Koltun, and Philipp Krähenbühl. “Tracking objects as points”. In: *ECCV*. 2020.

[103] Kuan Zhu, Haiyun Guo, Zhiwei Liu, et al. “Identity-Guided Human Semantic Parsing for Person Re-Identification”. In: *ECCV*. 2020.

## A Propagation

### A.1 Box Propagation

In order to propagate bounding boxes, we adopt two methods relying on fully-convolutional Siamese networks [5], [65], [73]. Given a target image patch  $I_x$  that contains the object of interest, and a search image patch  $I_z$  (typically a larger search area in the next frame), the appearance model  $\phi$  processes both patches and outputs their feature maps  $x = \phi(I_x)$  and  $z = \phi(I_z)$ .

**Cross-correlation (XCorr) head.** As in SiamFC [5], we simply cross-correlate the two feature maps, obtaining the response map

$$g(x, z) = x \star z \quad (3)$$

Eq. 3 is equivalent to performing an exhaustive search of the pattern  $x$  over the search region  $z$ . The location of the target object can be determined by finding the maximum value of response map.

**Discriminative Correlation Filter (DCF) head.** The DCF head [65], [73] is similar to the XCorr head, with two major differences. The first one is that it involves solving a ridge-regression problem to find the template  $w = \omega(x)$  rather than using the original template  $x$ , so that the response map is given by

$$g(x, z) = \omega(x) \star z \quad (4)$$

More specifically, the DCF template  $w = \omega(x)$  is obtained by solving

$$\arg \min_w \|w \star x - y\|^2 + \lambda \|w\|^2, \quad (5)$$

where  $y$  is an ideal response (here represented as a Gaussian function peaked at the center) and  $\lambda \geq 0$  is the regularization coefficient typical of ridge regression. The solution to Eq. 5 can be computed efficiently in the Fourier domain [65], [73] as

$$\hat{w} = \frac{\hat{x} \odot \hat{y}^*}{\hat{x} \odot \hat{x}^* + \lambda} \quad (6)$$

where  $\hat{x} = \mathcal{F}(x)$  indicates the discrete Fourier Transform of  $x$ ,  $y^*$  represents the complex conjugate of  $y$  and  $\odot$  denotes the Hadamard (element-wise) product. The response map can be computed via inverse Fourier Transform  $\mathcal{F}^{-1}$ ,

$$g(x, z) = \hat{w} \star z = \mathcal{F}^{-1}(\hat{w} \odot z) \quad (7)$$

Another difference w.r.t the XCorr head is that it is effective to update the template online by simple moving average [73], i.e.,  $\hat{w}_t = \frac{\alpha \hat{x}_t \odot \hat{y}^* + (1-\alpha) \hat{x}_{t-1} \odot \hat{y}^*}{\alpha(\hat{x}_t \odot \hat{x}_t^* + \lambda) + (1-\alpha)(\hat{x}_{t-1} \odot \hat{x}_{t-1}^* + \lambda)}$ . In contrast, with the XCorr head every frame is compared against the first one, as the above strategy does not improve results.

As shown in Table 3 and Table 4 from the main paper, for the tested architectures and appearance models we can see a clear advantage of DCF over XCorr. Note that the difference was less significant in the original paper [65], although the experiments were done with a significantly different (and shallower) architecture and with crops containing less context.

**Hyperparameters.** Following common practice [5], [36], we provide the Correlation Filter with a larger region of context in the template patch. To be specific, the template patch  $I_x$  is determined by expanding the height and width of the target bounding box by  $k = 4.5$  times. The search patch is also determined by expanding the bounding box by same amount, and its center corresponds the latest estimated location of the target. To handle scale variation of the object, we consider  $s = 3$  different search patches at different scales (computed as  $0.0275^{\{-1, 0, 1\}}$ ) to which are attributed different penalties ( $0.985^{\{1, 0, 1\}}$ ). Template and search patches are cropped and resized to  $520 \times 520$ . This means that with a total stride of  $r = 8$ , we have feature maps of size  $65 \times 65$ . In the DCF head, we set the regularization coefficient to  $\lambda = 1e^{-4}$ , and the moving average momentum to  $\alpha = 1e^{-2}$ .

### A.2 Mask and Pose Propagation

In Section 2.3 we introduced the recursive mask propagation as  $z_t = K_{t-1}^t z_{t-1}$ . In practice, to provide more temporal context, we use a memory bank [29], [34] consisting of multiple former label maps as the source label  $z_m$  instead of a single label map  $z_{t-1}$ , i.e.  $z_t = K_m^t z_m$ . More specifically, the resulting source label map is obtained by concatenating all the label maps inside the memory bank,  $z_m \in [0, 1]^{Ms}$ , where  $s$  is the spatial size of a single label map and  $M$  is the size of the memory bank. The softmax computed for  $K_m^t$  is applied over all  $Ms$  points in the memory bank. The memory bank always includes the first frame of the video, together with the latest  $M - 1$  frames (we choose  $M = 6$ ). As suggested by MAST [34] and CRW [29], we restricts the source points considered for each target point to a local

Box prop. hyperparameters	Values	Mask/Pose prop. hyperparameters	Values
Template patch size	$512 \times 512$	Image size	Mask: $480 \times 640$ Pose: $320 \times 320$
Search patch size	$512 \times 512$	Softmax temperature $\tau$	0.05
Box expanding coefficient	4.5	Memory size $M$	6
# Scales $s$	3	Local attention radius $r$	12
Scale factors	$1.0275^{\{-1,0,1\}}$	$k$ for $k$ -nearest neighbor	10
Scale penalties	$0.985^{\{1,0,1\}}$	Gaussian variance coefficient $\eta$	0.01
Regularization coefficient $\lambda$	$1e^{-4}$		
Moving average momentum $\alpha$	$1e^{-2}$		

circle with radius  $r = 12$ . The hyperparameter  $k$  for the  $k$ -NN used when computing the transition matrix  $K_m^t$  is set to  $k = 10$ .

Propagating pose key points is cast as propagating the mask of each individual key point, represented with the widely adopted Gaussian belief maps [78]. Each Gaussian has mean equal to the corresponding keypoint’s location, and variance proportional to the subject’s body size  $\sigma = \max(\eta s_{body}, 0.5)$ . The body size is determined by,

$$s_{body} = \max(\max_p \{x_p\} - \min_p \{x_p\}, \max_p \{y_p\} - \min_p \{y_p\}) \quad (8)$$

where  $(x_p, y_p)$  are the coordinates of the  $p$ -th key point.

## B Association

### B.1 Association Algorithm

**Motion cues: object states and Kalman filtering.** We employ a Kalman filter with constant velocity and linear motion model to handle motion cues in algorithms of the *association* type. We assume a generic setting where the camera is not calibrated and the ego-motion is not known. The object *states* are defined in an eight-dimensional space  $(u, v, \gamma, h, \dot{u}, \dot{v}, \dot{\gamma}, \dot{h})$ , where  $(u, v)$  indicate the position of bounding-box center,  $h$  the bounding-box height and  $\gamma = \frac{h}{w}$  the aspect ratio. The latter four dimensions represent the respective velocities of the first four terms.

For the sake of simplicity, we convert mask representations to bounding boxes. Let the coordinates of “in-mask” pixels form a set  $\{(x_j, y_j) | j = 1, \dots, N\}$ , where  $N$  is the number of mask pixels. Then, the center of the corresponding bounding box is obtained by averaging these coordinates as  $(u, v) = \frac{1}{N} \sum_{j=1}^N (x_j, y_j)$ . We estimate the height of the bounding box as  $h = \frac{2}{N} \sum_{j=1}^N \|y_j - h\|_1$ . This estimation is analogous to the one suggested in the continuous case by Li *et al.* [39]. Consider a rectangle with scale  $(2w, 2h)$  whose center is located at the origin of a 2D coordinate plane; by integrating over the points inside of the rectangle, we have  $\frac{1}{h} \int_{-h}^h \|y\|_1 dy = \frac{2}{h} \int_0^h y dy = h$ . For objects represented as a pose  $s$ , we first convert pose keypoints to masks following Appendix B.2, and then convert masks to boxes.

For each incoming frame, the Kalman Filter [31] predicts current states of existing tracklets. If a new detection is associated to a tracklet, then the state of the detection is used to update the tracklet state. If a tracklet is not associated with any detection, its state is simply predicted without correction.

We use the (squared) Mahalanobis distance [80] to measure the “motion distance” between a newly arrived detection and an existing tracklet. Let us project the state distribution of the  $i$ -th tracklet into the measurement space and denote mean and covariance as  $\mu_i$  and  $\Sigma_i$ , respectively. Then, the *motion distance* is given by

$$c_{i,j}^m = (\mathbf{o}_j - \mu_i)^\top \Sigma_i^{-1} (\mathbf{o}_j - \mu_i) \quad (9)$$

where  $\mathbf{o}_j$  indicates the observed (4D) state of the  $j$ -th detection. We observe that the Mahalanobis distance consistently outperforms Euclidean distance and IOU distance, likely thanks to the consideration of state estimation uncertainty. Using this metric also allows us to filter out unlikely matches by simply thresholding at 95% confidence interval [80]. We denote the filtering with an indicator function

$$b_{i,j} = \mathbb{1}[c_{i,j}^m > \eta]. \quad (10)$$

The threshold  $\eta$  can be computed from the inverse  $\mathcal{X}^2$  distribution. In our case the degrees of freedom of the  $\mathcal{X}^2$  distribution is 4, so the threshold  $\eta = 9.4877$ .

**Algorithm 1:** Hungarian Association

---

**Input:** Tracklet indices  $\mathcal{T} = \{1, \dots, N\}$ , detection indices  $\mathcal{D} = \{1, \dots, M\}$ . Hyperparameter  $\lambda$ .  
**Output:** Set of matches  $\mathcal{M}$ , set of unmatched tracklets  $\mathcal{T}_{remain}$ , and detections  $\mathcal{D}_{remain}$

```

1 Initialization:  $\mathcal{M} \leftarrow \emptyset$ ,  $\mathcal{D}_{remain} \leftarrow \mathcal{D}$ ,  $\mathcal{T}_{remain} \leftarrow \mathcal{T}$  ;
2 for  $t \in \mathcal{T}$  do
3   | Predict the state of the  $t$ -th tracklet using Kalman Filter
4 end
5   // main matching stage
6 Compute motion cost matrix  $\mathbf{C}^m = [c_{i,j}^m]$  using Eq. 9;
7 Compute appearance cost matrix  $\mathbf{C}^a = [c_{i,j}^a]$  using Eq. 11;
8 Compute final cost matrix  $\mathbf{C} = \lambda \mathbf{C}^a + (1 - \lambda) \mathbf{C}^m$ ;
9  $[x_{i,j}] = \text{Hungarian\_assignment}(\mathbf{C})$ ;
10  $\mathcal{M} \leftarrow \mathcal{M} \cup \{(i, j) | b_{i,j} \cdot x_{i,j} > 0\}$  ;
11  $\mathcal{T}_{remain} \leftarrow \mathcal{T} \setminus \{i | \sum_j b_{i,j} \cdot x_{i,j} > 0\}$  ;
12  $\mathcal{D}_{remain} \leftarrow \mathcal{D} \setminus \{j | \sum_i b_{i,j} \cdot x_{i,j} > 0\}$  ;
13   // second matching stage
14 Compute IOU cost matrix  $\mathbf{C}^g$  between  $\mathcal{T}_{remain}$  and  $\mathcal{D}_{remain}$  ;
15  $[x_{i,j}] = \text{Hungarian\_assignment}(\mathbf{C})$ ;
16  $\mathcal{M} \leftarrow \mathcal{M} \cup \{(i, j) | x_{i,j} > 0\}$  ;
17  $\mathcal{T}_{remain} \leftarrow \mathcal{T}_{remain} \setminus \{i | \sum_j x_{i,j} > 0\}$  ;
18  $\mathcal{D}_{remain} \leftarrow \mathcal{D}_{remain} \setminus \{j | \sum_i x_{i,j} > 0\}$  ;

```

---

**Association algorithm.** Algorithm 1 outlines the association procedure for a *single timestamp*. The algorithm takes as input a set of tracklets  $\mathcal{T} = \{1, \dots, N\}$  and detections  $\mathcal{D} = \{1, \dots, M\}$ . First, we predict the current states of the all tracklets using the Kalman Filter. Then we perform the main matching stage. During this stage, we compute a motion cost matrix  $\mathbf{C}^m$  using Eq 9, and compute an appearance cost matrix  $\mathbf{C}^a$  using the RSM metric described in Section 2.4,

$$c_{i,j}^a = \text{RSM}(i, j) \quad (11)$$

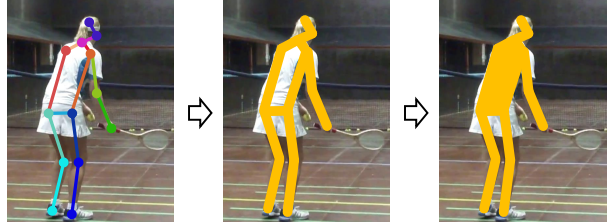
The final cost matrix is the linear combination of the two cost matrices  $\mathbf{C} = \lambda \mathbf{C}^a + (1 - \lambda) \mathbf{C}^m$ . We set  $\lambda = 0.99$ . A Hungarian solver takes the cost matrix  $\mathbf{C}$  as input and outputs matches  $[x_{i,j}]$ . We then filter out unrealistic matches using Eq 10. For the remaining tracklets and detections which failed matching, we perform a second matching stage using IOU distance as the cost matrix. Remaining tracklets and detections are output by the association algorithm. Further steps (described below) determine if a remaining tracklet should be terminated or if a new identity should be initialized from a remaining detection.

**Tracklet termination and initialization.** If a tracklet fails to be matched with a newly arrived detection with Algorithm 1, we mark it as *inactive*. To account for short occlusions, inactive tracklets can still be restored if they are found to be matching with a new detection. We record a timer for each inactive tracklet. Once a timer reaches 1 second, its corresponding tracklet is removed from the tracklet pool.

If a detection fails to match existing tracklets with Algorithm 1, it could correspond to a new tracklet. However, this would result in the creation of frequent brief “spurious” tracklets, containing one detection only. To cope with this issue, similarly to [80] we only initialize a new tracklet if a new detection appears in two consecutive frames.

## B.2 Pose-to-Mask Conversion

Given the key points’ location of a target person, we convert the pose into a binary mask in two steps. First, the key points are connected to form a skeleton, where the width of each segment forming this skeleton is proportional to the body size with a linear coefficient  $\eta_p = 0.05$ , and the body size is computed with Eq. 8. Second, we fill closed polygons inside the pose skeleton, since the parts inside the polygon usually belong to the target object.



Detector	DPM			FRCNN			SDP			FairMOT-Det			w/ motion
	Metrics	IDF1	IDs	MOTA									
CF	36.5	748	<u>29.8</u>	51.3	480	<b>50.2</b>	60.9	848	64.5	75.5	550	<b>82.9</b>	✓
GPF	34.4	1261	29.3	50.0	530	<b>50.2</b>	60.8	985	<b>64.8</b>	76.4	<u>534</u>	<b>82.9</b>	✓
GF	36.3	674	<u>29.8</u>	52.2	479	<b>50.2</b>	62.0	<u>759</u>	<u>64.6</u>	75.9	<u>499</u>	<b>82.9</b>	✓
ReID	<b>40.0</b>	<u>619</u>	<u>29.8</u>	<u>54.9</u>	<u>461</u>	<u>50.1</u>	<b>67.1</b>	811	64.5	<u>78.4</u>	545	<u>82.8</u>	✓
RSM	<u>39.6</u>	<b>513</b>	<b>30.0</b>	<b>55.6</b>	<b>431</b>	<b>50.2</b>	<u>64.2</u>	<u>762</u>	64.5	<b>78.6</b>	543	82.7	✓
CF	26.3	1381	22.8	40.4	820	47.4	46.7	1525	58.2	60.4	1599	76.6	
GPF	<u>29.5</u>	<u>782</u>	<u>25.5</u>	43.7	<u>517</u>	<u>48.2</u>	48.8	1337	59.5	57.2	1414	77.4	
GF	24.9	1298	22.4	41.7	526	48.1	51.0	<b>960</b>	<u>60.6</u>	<u>65.3</u>	<u>868</u>	<u>78.9</u>	
ReID	<b>33.1</b>	<b>637</b>	<b>25.9</b>	<u>47.0</u>	692	47.5	<u>53.3</u>	1250	58.5	64.8	1448	75.9	
RSM	28.1	805	25.4	<b>51.5</b>	<b>414</b>	<b>49.8</b>	<b>58.6</b>	<u>999</u>	<b>62.7</b>	<b>74.5</b>	<b>605</b>	<b>82.3</b>	

**Table 5:** Comparison between different similarity metrics for association, tested on MOT-16 *train* split. We provide results that (1) use motion cues and (2) discard motion cues. The best results are **bolded** and the second best results are underlined.

Methods	IDF1	IDs	MOTA
CF	38.6	6384	<b>41.8</b>
GPF	38.3	6245	<b>41.8</b>
GF	<u>39.3</u>	<u>5858</u>	<b>41.8</b>
ReID	39.1	6442	<u>41.7</u>
RSM	<b>41.3</b>	<b>5552</b>	41.6

**Table 6:** Comparison between different similarity metrics for association, tested on MOT-20 [14] with the provided detector.

Methods	IDF1	IDs	sMOTSA
CF	62.8	1529	80.7
GPF	60.7	1071	82.4
RSM	<b>66.5</b>	<b>808</b>	<b>83.4</b>

**Table 7:** Comparison between different similarity metrics for *association*, tested on MOTS [69] *train* split based on the segmentation masks provided by the COSTA<sub>st</sub> [12] tracker.

## C Ablations for the Reconstruction Similarity Metric (RSM)

In Section 2.4 we claimed that the good tracking performance of UniTrack on association-type tasks is largely attributed to the proposed Reconstruction Similarity Metric (RSM). In this section, we provide results of several baseline methods in order to validate its effectiveness. These baseline are described below.

**Center feature (CF).** For a given observation feature  $d_j \in \mathbb{R}^{s_{d_j} \times C}$  of a bounding box or a mask, we compute the location of its center of mass and extract the corresponding point feature (a single  $C$ -dim vector) as representation of this observation. Cosine similarity is computed to measure how likely two observations belong to the same identity. Using CF to represent an object is a straightforward strategy, widely used in tracking tasks [77], [98], [102]. The benefit of CF is that it can handle objects in any observation format, *e.g.* boxes or masks, while the clear drawback is that it cannot represent an object in its entirety.

**Global feature (GF).** For a given observation feature  $d_j \in \mathbb{R}^{s_{d_j} \times C}$ , we concatenate the  $s_{d_j}$  point features and obtain a single global feature vector with length  $s_{d_j}C$ . Cosine similarity is computed to measure how likely two observations belong to the same identity. Note that only representations with fixed  $s_{d_j}$  are feasible in this case. For this reason, we only provide results for GF on the MOT task, where observations are bounding boxes that can be resized to a fixed size. The benefit of GF is that it preserve complete information of the observation, while the main drawback is that local features may not align across samples. Therefore, global feature is most applicable in cases where samples are aligned with a pre-processing step, *e.g.* in face recognition [20].

**Global-pooled feature (GPF)** is computed similarly to the global feature, but with averaging being performed along the  $s_{d_j}$  dimension to obtain a single feature vector with length  $C$ . Cosine similarity is then computed to measure how likely it is that the two observations belong to the same identity. This strategy is adopted by many (ReID) approaches [61], [62], [103] and has similar benefits and drawbacks to the center feature.

**Supervised ReID feature (ReID).** For a given image cropped from a bounding box, we employ a strong, off-the-shelf person ReID model to extract a single feature vector with length  $C$ , and compute cosine similarity between observations. The model uses a ResNet-50 [27] architecture and is trained with the joint set of three widely-used datasets: Market-1501 [100], CUHK-03 [38], and DukeMTMC-ReID [56]. Using supervised ReID models to extract appearance features is widely used in existing multi-object tracking approaches [43], [57], [63]. Given that large amount of identity labels are leveraged during training, supervised ReID models usually show good association accuracy.

Methods	PCK@0.1	PCK@0.2
TimeCycle [76]	57.3	78.1
UVC [39]	58.6	79.6
CRW [29]	<b>59.0</b>	<b>83.2</b>
I18 (reported in [29])	53.8	74.6
I18 (UniTrack)	58.3	80.5
Yang et al. [91]	<b>68.7</b>	<b>92.1</b>

**Table 8:** Results of pose propagation on JHMDB [30] dataset. I18 refers to using ImageNet pre-trained ResNet-18 as the appearance model.

Methods	mAP $\uparrow$
FEELVOS [68]	26.9
SipMask [6]	<b>32.5</b>
OSMN $^\dagger$ [92]	27.5
DeepSORT $^\dagger$ [80]	26.1
MTRCNN $^\dagger$ [90]	30.3
UniTrack $^\dagger$	30.1

**Table 9:** VIS results@YoutubeVIS [90] *val* split.  $^\dagger$  indicates methods using the same observations (segmentation masks in every single frames).

Note that for CF, GF, GPF, and the proposed RSM, we employ the same appearance model (ImageNet pre-trained ResNet-18) for fair comparison. For a broad comparison, we provide results obtained with different detectors and on different datasets. We adopt the following detectors and test on MOT-16 [47] *train* split (listed with detection accuracy from low to high): DPM [21], Faster R-CNN [55] (FRCNN), SDP [89], and FairMOT [98].

Results are shown in Table 5. We first apply the full association algorithm, *i.e.* using both appearance and motion cues. In this case (first half of the table), RSM consistently outperforms CF, GF, GPF baselines, and even surpasses the supervised ReID features in several cases, *e.g.* with FRCNN and FairMOT detectors. In the second half of the table, we show results in which only appearance cues are used, so that the difference between metrics (which are based on appearance) can be better emphasized. In this case, the gaps between different methods are more significant than in the previous case, and RSM still consistently outperforms CF, GF, and GPF. Furthermore, RSM also surpasses the strong supervised ReID feature with all detectors, except for DPM. This suggests that RSM can be an effective similarity metric for tasks that have *association* at their core.

To show the generality of the results, we also experiment on different datasets and different tasks. Table 6 shows comparisons on the MOT-20 [14] *train* split for the MOT task (box observations). The MOT-20 dataset focuses on very crowded MOT scenes. Table 7 presents results on MOTS [69] *train* split for the MOTS task (mask observations). Note for the MOTS task, since the masks vary in size, it is not feasible to apply the GF strategy. Results show that the proposed RSM yields significantly higher IDF1 scores on both datasets.

## D More Tracking Tasks

In this section we present two more tasks that UniTrack can address.

The first task is **human Pose Propagation** on the JHMDB [30] dataset: each video contains a *single* person of interest, and the pose keypoints are provided in the first frame of the video only. The goal here is to predict the pose of the person throughout the video. Note that this is different from the previously mentioned PoseTrack task: PoseTrack mainly focuses on association between different identities, while in Pose Propagation we aim at propagating the pose of a single identity.

Results are shown in Table 8. We report a higher result with ImageNet pre-trained ResNet-18 compared with in previous work [29], [39] (58.3 *v.s.* 53.8 PCK@0.1). With this result, we observe the best self-supervised method CRW [29] does not beat the ImageNet pre-trained representation by a significant margin (only +0.7 PCK@1). This again validates our second finding in Section 3.2: a vanilla ImageNet-trained representation is surprisingly effective.

The second task is **Video Instance Segmentation (VIS)**. The problem of VIS is similar to Multiple Object Tracking and Segmentation (MOTS), but its setup differs in the following aspects: first, the object categories are fairly diverse (40 different categories), while in MOTS objects are mostly persons and vehicles. This also requires the trackers tackling the VIS task to handle objects from different classes within the same scene. Second, the evaluation metrics are different. In MOTS, the MOT-like metrics (CLEAR [4], IDF-1/IDs, and HOTA [45]) are used, which implicitly encourages methods to focus on outputting temporally consistent trajectories. Instead, for VIS the evaluation metric is spatial-temporal mAP, a temporal extension of the vanilla mAP which is usually used in detection and segmentation tasks. The mAP metric significantly biases towards segmentation and classification accuracy in single frames, thus being less informative for evaluating “tracking” accuracy.

Results on VIS task are shown in Table 9. We adopt an identical segmentation model to the one of MaskTrackRCNN [90], and observe only a 0.2 difference in mAP. For further comparison, we also provide results of two other association

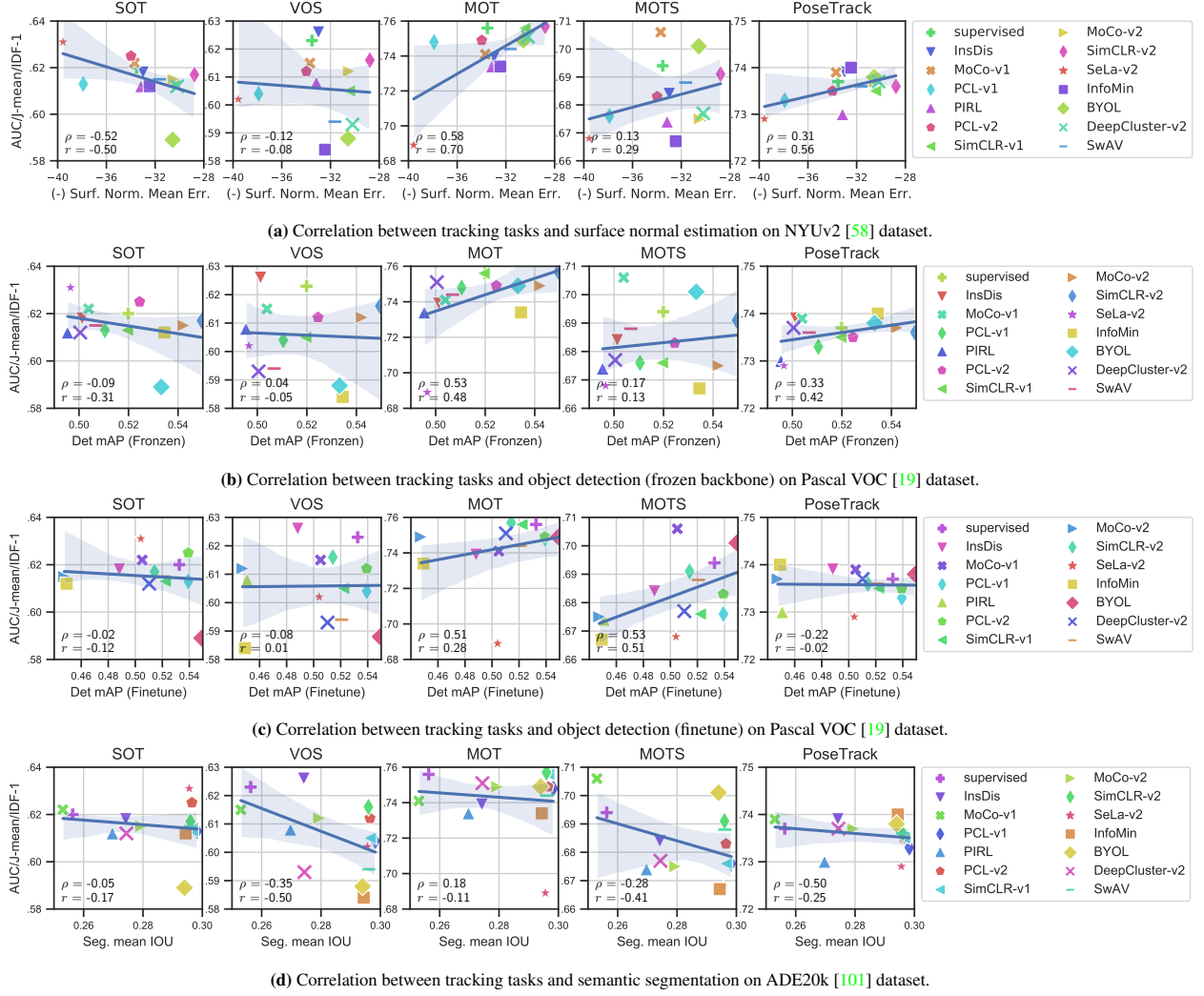


**Figure 7:** Correlation study between tracking tasks and other tasks for SSL models. On the y-axes we plot tracking performance, and on x-axes performance of the other tasks. Spearman’s  $r$  and Pearson’s  $\rho$  are shown in the left bottom corner of each plot, indicating how the two axes are correlated.

methods, OSMN [92] and DeepSORT [80], providing them with the same observations as used by UniTrack. Note how UniTrack boasts better accuracy than both methods (30.0 v.s. 27.5 and 26.1 mAP). Our results is also competitive with the state-of-the-art SipMask [6], with only  $-2.4$  points of mAP.

## E Additional Correlation Studies

In Section 3.2, we investigated the correlation between tracking performance and ImageNet “linear probe” accuracy for different SSL models. In this section, we provide more results and discussions by studying the correlation between tracking performance and several other downstream tasks when using the appearance model from the many SSL methods under consideration. For non-tracking tasks, we report numbers from [18]. Results are shown in Figure 7.

We report three tasks: surface normal estimation on the NYUv2 [58] dataset, where the *negative* mean angular error is used as evaluation metric; Object detection on Pascal VOC [19], with performance measured in mAP; Semantic segmentation on ADE20k [101] dataset, with performance measured in mean IOU . In each subplot, we plot the performance of five tracking tasks along the y-axes, and performance of the other task along the x-axes. Higher numbers are better along both the two axes in all the plots. As in the main paper, we compute two types of correlation coefficient: Spearman’s  $r$  and Pearson’s  $\rho$ , and report them in the left bottom corner of each plot. Several interesting findings can be observed:

(a) *Correlation between tracking and surface normal prediction performance is fairly strong.* Results are shown in Figure 7a. For instance,  $r = 0.70$  for surface normal error v.s. MOT accuracy, and  $0.56$  for surface normal error v.s. PoseTrack accuracy. Interestingly, the behavior of SOT is in contrast with MOT and PoseTrack: SOT accuracy is moderately negative correlated ( $r = -0.50$ ) with surface normal estimation accuracy. VOS presents a similar trend to the one of SOT, but with a lower correlation coefficient.

(b) *Object detection is moderately correlated with association-type tracking tasks.* For object detection, we consider two setups: one is to freeze the representation and only train the additional classification/regression head; the other is to finetune the whole network in an end-to-end manner. Results are shown in Figure 7b and 7c respectively. In general, MOT and PoseTrack are moderately correlated with object detection under the frozen setting ( $r = 0.48$  for MOT and  $r = 0.42$  for PoseTrack), and MOTS is moderately correlated with object detection under the finetune setting ( $r = 0.51$ ). Propagation-type tasks are poorly correlated with object detection results under both settings ( $|\rho| < 0.10$ ). We speculate that, in this case, positive correlation might be due to the fact that both object detection and association-type tracking require discriminative features at the level of the object.

(c) *Semantic segmentation is slightly negative correlated with tracking tasks.* As can be observed in Figure 7d, correlation coefficients between segmentation accuracy and tracking performance are mildly negative. Among these results, VOS is the task that is most (negatively) correlated with segmentation (with a severe case of  $r = -0.50$  only for the ADE20k dataset). MOTS and PoseTrack are also mildly correlated, with  $r = -0.41$  and  $r = -0.25$  respectively. We speculate that negative correlation might be cause to the fact that tracking and segmentation require features with contradictory properties. Consider two different instances that belongs to the same category, *i.e.* two different pedestrian. For segmentation, the task requires pixel-wise classification, meaning that pixels inside the two instances should be equally classified into the same “pedestrian” class, thus their features should be *similar* (close to the class center). In contrast, for tracking tasks, it is required to distinguish different instances from the same class, otherwise a tracker would easily fail when objects overlap with each other. Therefore, point features inside the two different pedestrian are expected to be *dissimilar*.